Electronic Supporting Information

Heterometallic $Cu^{II}Fe^{III}$ and $Cu^{II}Mn^{III}$ Alkoxo-Bridged Complexes Revealing a Rare Hexanuclear $M_6(\mu\text{-}X)_7(\mu_3\text{-}X)_2$ Molecular Core

Oksana V. Nesterova,[a] Dmytro S. Nesterov,*[a] Beáta Vranovičová,[b] Roman Boča[b] and Armando J. L. Pombeiro,*[a]*

[a] Centro de Química Estrutural, Complexo I, Instituto Superior Técnico, Universidade de Lisboa, Avenida Rovisco Pais, 1049-001 Lisboa, Portugal; e-mails: oksana.nesterova@tecnico.ulisboa.pt, dmytro.nesterov@tecnico.ulisboa.pt; pombeiro@tecnico.ulisboa.pt

[b] Department of Chemistry, FPV, University of SS Cyril and Methodius, 917 01 Trnava, Slovakia

Contents

Table S1. Selected geometrical parameters (distances/Å and angles/°) for **1** and **2**.

	1	**2**		**1** (M = Fe)	**2** (M = Mn)
Cu1–O1	1.968(2)	1.984(7)	Cu4–O6	2.023(2)	1.982(7)
Cu1–O2	1.990(2)	1.995(7)	Cu4–O7	1.877(2)	1.882(7)
Cu1–O4	1.913(2)	1.921(7)	Cu4–O8	2.176(2)	2.206(7)
Cu1–O16	1.952(3)	1.961(7)	Cu4–O13	1.928(2)	1.938(7)
Cu1–N1	2.404(3)	2.438(10)	Cu4–N4	2.122(3)	2.082(9)
Cu2–O1	2.535(2)	2.480(7)	M1–O1	1.980(2)	1.975(7)
Cu2–O3	1.981(2)	1.988(8)	M1–O3	1.959(2)	1.854(7)
Cu2–O4	1.937(2)	1.935(8)	M1–O5	1.974(2)	1.886(7)
Cu2–O9	1.973(3)	1.952(7)	M1–O10	2.019(2)	2.146(8)
Cu2–N2	2.615(3)	2.521(10)	M1–O11	2.072(3)	1.999(8)
Cu2–Cl1	2.2548(11)	–	M1–O23	2.029(2)	2.185(8)
Cu2–Cl1B	–	2.194(9)	M2–O2	1.938(2)	1.889(8)
Cu3–O5	1.929(2)	1.976(7)	M2–O6	2.105(2)	2.296(7)
Cu3–O6	2.065(2)	1.991(7)	M2–O8	1.924(2)	1.871(7)
Cu3–O7	1.923(2)	1.938(7)	M2–O14	2.079(2)	1.995(7)
Cu3–O12	1.950(2)	1.941(8)	M2–O15	2.050(3)	2.113(7)
Cu3–N3	2.315(3)	2.349(9)	M2–O23	1.989(2)	1.945(8)
O1–Cu1–O2	90.52(10)	89.1(3)	O6–Cu4–O7	81.94(10)	82.1(3)
O1–Cu1–O4	84.66(10)	83.7(3)	O6–Cu4–O8	80.86(9)	82.7(3)
O1–Cu1–O16	167.19(10)	167.6(3)	O6–Cu4–O13	93.58(10)	92.2(3)
O1–Cu1–N1	82.73(10)	81.5(3)	O6–Cu4–N4	159.06(10)	161.5(3)
O2–Cu1–O4	172.23(10)	172.6(3)	O7–Cu4–O8	96.60(10)	96.0(3)
O2–Cu1–O16	90.89(10)	94.1(3)	O7–Cu4–O13	161.96(10)	163.6(3)
O2–Cu1–N1	78.58(10)	77.9(3)	O7–Cu4–N4	86.54(11)	87.0(3)
O4–Cu1–O16	92.48(10)	92.5(3)	O8–Cu4–O13	99.94(10)	98.5(3)
O4–Cu1–N1	106.75(10)	102.8(3)	O8–Cu4–N4	83.18(10)	83.6(3)
O16–Cu1–N1	110.03(11)	110.8(3)	O13–Cu4–N4	102.48(11)	102.1(3)
O1–Cu2–O3	72.10(8)	69.9(3)	O1–M1–O3	86.34(10)	85.1(3)
O1–Cu2–O4	70.09(9)	71.1(3)	O1–M1–O5	94.87(10)	93.9(3)
O1–Cu2–O9	99.65(9)	101.5(3)	O1–M1–O10	91.83(10)	91.1(3)
O1–Cu2–Cl1	107.79(6)	–	O1–M1–O11	173.72(10)	172.5(3)
O1–Cu2–Cl1B	–	105.4(3)	O1–M1–O23	92.30(10)	89.6(3)
O1–Cu2–N2	132.04(8)	133.6(3)	O3–M1–O5	178.73(10)	178.3(3)
O3–Cu2–O4	90.71(10)	90.4(3)	O3–M1–O10	88.91(10)	88.3(3)
O3–Cu2–O9	84.76(11)	87.3(3)	O3–M1–O11	87.49(10)	87.4(3)
O3–Cu2–Cl1	173.51(8)	–	O3–M1–O23	93.07(10)	94.9(3)
O3–Cu2–Cl1B	–	169.4(3)	O5–M1–O10	90.68(10)	90.4(3)
O3–Cu2–N2	76.54(10)	77.3(3)	O5–M1–O11	91.31(10)	93.6(3)
O4–Cu2–O9	169.67(10)	172.6(3)	O5–M1–O23	87.27(9)	86.5(3)
O4–Cu2–Cl1	95.34(8)	–	O10–M1–O11	89.21(10)	88.8(3)
O4–Cu2–Cl1B	–	97.1(3)	O10–M1–O23	175.53(10)	176.8(3)
O4–Cu2–N2	75.05(10)	77.3(3)	O11–M1–O23	86.87(10)	90.8(3)
O9–Cu2–Cl1	88.89(8)	–	O2–M2–O6	95.51(10)	94.0(3)
O9–Cu2–Cl1B	–	84.3(3)	O2–M2–O8	177.11(10)	173.1(3)
O9–Cu2–N2	112.70(10)	109.0(3)	O2–M2–O14	90.69(10)	92.2(3)
N2–Cu2–Cl1	107.27(7)	–	O2–M2–O15	90.83(10)	92.9(3)
N2–Cu2–Cl1B	–	111.6(3)	O2–M2–O23	88.52(10)	85.5(3)
O5–Cu3–O6	93.60(10)	94.4(3)	O6–M2–O8	85.01(10)	82.7(3)
O5–Cu3–O7	171.95(10)	174.1(3)	O6–M2–O14	85.06(9)	85.0(3)
O5–Cu3–O12	93.89(10)	92.9(3)	O6–M2–O15	171.48(10)	171.4(3)
O5–Cu3–N3	80.92(10)	79.7(3)	O6–M2–O23	89.71(9)	88.0(3)
O6–Cu3–O7	79.78(10)	80.5(3)	O8–M2–O14	92.19(10)	93.6(3)

O6–Cu3–O12	161.67(10)	167.0(3)	O8–M2–O15	88.94(10)	90.9(3)
O6–Cu3–N3	83.16(10)	82.8(3)	O8–M2–O23	88.65(10)	88.3(3)
O7–Cu3–O12	91.17(10)	91.6(3)	O14–M2–O15	89.18(10)	89.6(3)
O7–Cu3–N3	102.63(10)	102.5(3)	O14–M2–O23	174.61(10)	172.5(3)
O12–Cu3–N3	114.55(10)	109.1(3)	O15–M2–O23	96.16(10)	97.6(3)

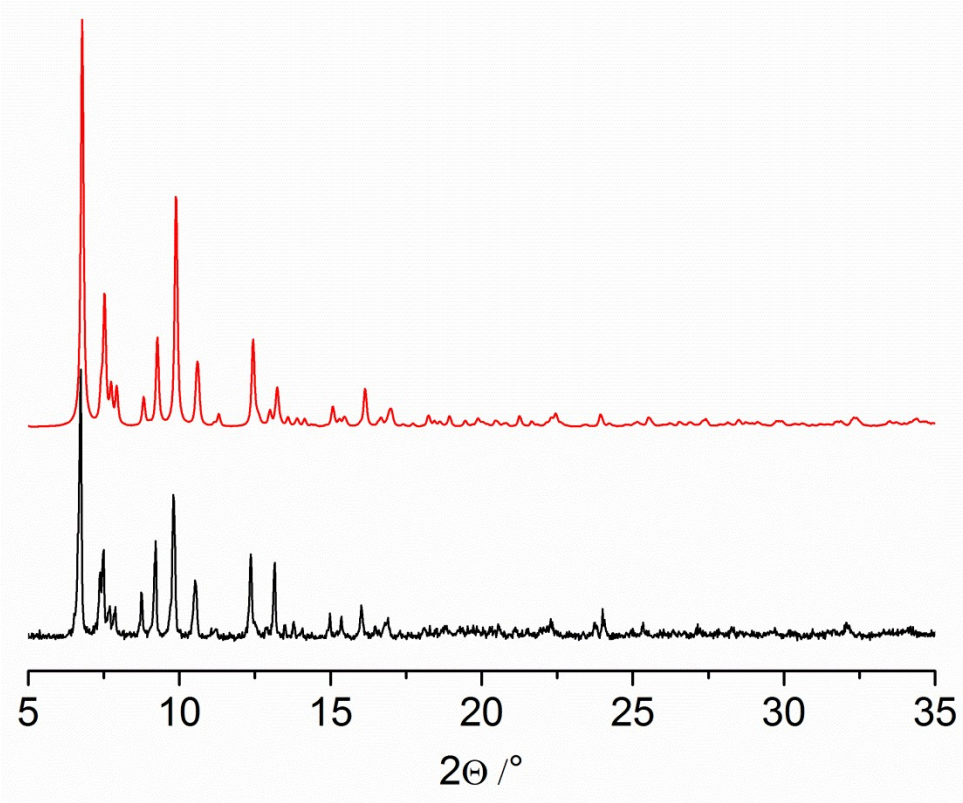

Figure S1. Calculated (top) and experimental (bottom) powder X-day plots for **1**.

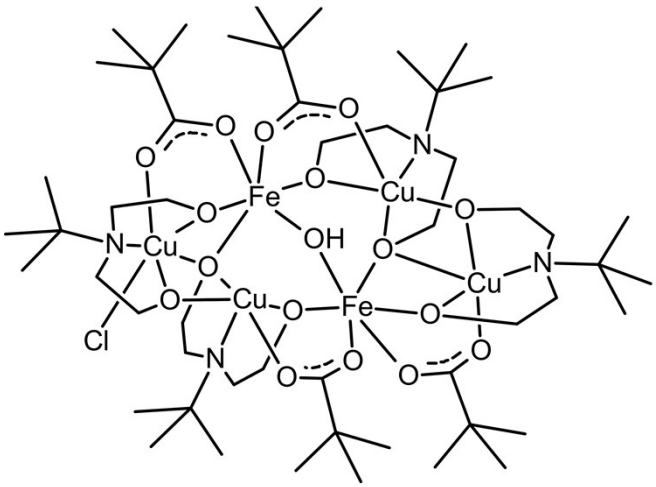

Figure S2. Schematic representation of the molecular structure of **1**.

The analysis of the {$M_6(\mu\text{-}X)_7(\mu_3\text{-}X)_2$}Molecular Structure Type (MST)

The analysis of the Molecular Structure Type (MST)[1] {$M_6(\mu\text{-}X)_7(\mu_3\text{-}X)_2$} of **1** and **2** (Figure 2) reveals that it can be represented as a combination of two $M_3(\mu\text{-}X)_2(\mu_3\text{-}X)$ fragments joined together by three bridging oxygen atoms. It was interesting to study in the CSD[2] the combinations of $M_3(\mu\text{-}X)_2(\mu_3\text{-}X)$ fragments other than that in **1** and **2**. All structures can be classified into two groups, according to the number of sub-structures (fragments) $M_3(\mu\text{-}X)_2(\mu_3\text{-}X)$ found in the respective MST: one fragment (Table S2) and two fragments (Table S3). In the first group (Table S2), all molecular cores of the hexanuclear complexes are based on the trimetallic $M_3(\mu\text{-}X)_2(\mu_3\text{-}X)$ fragment. The MSTs *a* {$M_6(\mu\text{-}X)_2(\mu_3\text{-}X)_4$} and *b* {$M_6(\mu\text{-}X)_4(\mu_3\text{-}X)(\mu_5\text{-}X)$} are observed in the structures of the heterometallic $[Et_4N]_2[(OWS_3Cu_2)_2(pydt)_2]$ (Hpydt = 2-pyridinethiol) and $[Ag_4W_2S_8(C_{25}H_{22}P_2)_3]\cdot 2C_3H_7NO$ compounds, respectively (CSD refcodes WOJYEA and KUYRIG), and contain the lowest number (six) of the bridging (sulphur) atoms within molecular cores.[3] The main difference between them is the way of the coordination of the similar M_3X_3 lateral part to the main $M_3(\mu\text{-}X)_2(\mu_3\text{-}X)$ moiety: in *a* the coordination occurs *via* two μ_3-X atoms, while in *b* it is *via* μ_5-X. Moreover, in *b* the μ_5-X atom completes the $M_3(\mu\text{-}X)_2(\mu_3\text{-}X)$ moiety into the incomplete cube-like $M_3(\mu\text{-}X)_3(\mu_3\text{-}X)$ fragment, which is one of the widespread fragments found in the different molecular cores. The MST *c* {$M_6(\mu\text{-}X)_9(\mu_3\text{-}X)$} is found in the organodiphosphonate derivative $(TBA)_3[(O_3PCOHCH_3PO_3)Mo_6O_{18}H(DMF)]\cdot 4.5H_2O$ (refcode XEGFIA) and it is formed with the participation of the largest number of μ-X bridging atoms showing an open-textured core structure.[4] Among the studied compounds, the largest number of bridging atoms, 12, and the most complex molecular core is observed in the MST *d* {$M_6(\mu\text{-}X)_9(\mu_3\text{-}X)_3$}, which occurs in a molybdenum complex with S-bridges. Similarly to MST *b*, in *d* the formation of the incomplete cube-like $M_3(\mu\text{-}X)_3(\mu_3\text{-}X)$ fragment *via* the direct coordination of the μ-X atom to the trimetallic fragment is observed.

Table S2. Geometries of M_nX_m coordination cores, based on the $M_3(\mu\text{-}X)_2(\mu_3\text{-}X)$ fragment (shown as dark blue).

	MST	*N*D*k*-*m* symbol	Structure
a	$\{M_6(\mu\text{-}X)_2(\mu_3\text{-}X)_4\}$	2,3,4,4M6-1	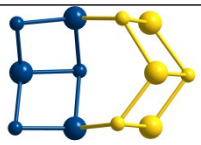
b	$\{M_6(\mu\text{-}X)_4(\mu_3\text{-}X)(\mu_5\text{-}X)\}$	2,4,4,5M6-1	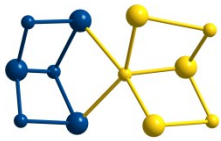
c	$\{M_6(\mu\text{-}X)_9(\mu_3\text{-}X)\}$	2,2,3,3,3,4M6-1	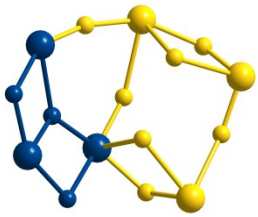
d	$\{M_6(\mu\text{-}X)_9(\mu_3\text{-}X)_3\}$[a]	2,2,3,4M6-1	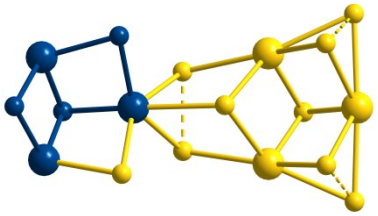

[a] The dashed lines in *d* show the contacts X–X and are not taking into account in MST definition.

All complexes in the second group contain two $M_3(\mu\text{-}X)_2(\mu_3\text{-}X)$ fragments which are linked into an hexanuclear core by different number of bridging atoms (Table S3). In the MST *e* $M_6(\mu\text{-}X)_7(\mu_3\text{-}X)_2$ the main trimetallic fragments are joined by one bridging atom, what is observed in $[Mo_3S_4(HBpz_3)_2]_2(\mu\text{-}O)(\mu\text{-}C_3H_3N_2)_2$ (CSD refcode JAFLAD).[5] A determining role in the formation of such molecular structure conceivably is the presence of rigid bulky pyrazole-containing ligands, which, being coordination to the Mo atoms, surround the overall hexanuclear core. In the MST *f* $M_6(\mu\text{-}X)_8(\mu_3\text{-}X)_2$, two atoms joining metal-containing trimetallic moieties are present. Moreover, in both cases, besides bridging atoms between $M_3(\mu\text{-}X)_2(\mu_3\text{-}X)$ fragments, also bridging atoms that directly bond to the trimetallic cores forming incomplete cube-like geometry were observed. The MST *f* is found in the

$[W_6O_4Cl_{10}]^{2-}$ anion structure (refcode JIYMIN) and in $[Mo_6O_{10}(bpy)_4(Hnta)_2]$ (refcode OZOQEA; nta = nitrilotriacetate).[6]

In the MSTs *g* $\{M_6(\mu\text{-}X)_7(\mu_3\text{-}X)_2\}$ (found in the complexes **1** and **2**), *h* $\{M_6(\mu\text{-}X)_9(\mu_3\text{-}X)_2\}$ and *i* $\{M_6(\mu\text{-}X)_6(\mu_3\text{-}X)_2(\mu_4\text{-}X)\}$ three bridging atoms are responsible for combining $M_3(\mu\text{-}X)_2(\mu_3\text{-}X)$ fragments into hexanuclear cores. Apart from **1** and **2**, the MST *g* is also observed in the structure of $[N(CH_3)_4]_4[\{H(SO_4)W_3O_7(O_2)_2\}_2O]$ (refcode TALPAX), while MST *h* is found in a molybdenum compound with O, Cl and S bridging atoms (refcode MIWFOP).[7, 8] The MST *i*, formed using a μ_4-X bridging atom, is the most widespread MST in the performed search (24 hits in CSD) covering the majority of hexanuclear molecular cores based on $M_3(\mu\text{-}X)_2(\mu_3\text{-}X)$ fragments. All the compounds belonging to the MST *i* are S/Se-bridged mono- or heterometallic iron-containing clusters revealing close-packed metal cores.

It should be noted that, formally, MSTs *e* and *g* have the same $\{M_6(\mu\text{-}X)_7(\mu_3\text{-}X)_2\}$ formulae, but they are different from the topological point of view. In general, the coordination core of the complex can be represented as a graph, which vertexes are metal centres M and edges are any metal pairs linked by bridging atoms, M–X–M. Such a simplification is useful in the classification of the metal core topologies.[1a, 9] So, the topology of the metal core M_aX_b can be written as a graph $G = (V, E)$, where V = a and the number of edges E should be further estimated, assuming any M–X–M bridging as an edge.[9a, 9c] More particularly, the topology of the metal core M_aX_b can be written using the *N*D*k*-*m* symbol, where *N* is a sequence of coordination numbers of topologically non-equivalent graph vertexes (metal centres), D is dimensionality of the coordination network (written as "M" for molecular clusters), *k* is the number of graph vertexes (metal atoms) in the core, and *m* is an ordering number to distinguish topologically different clusters having the same *N*D*k* symbol. The combination of these alternative approaches and using MST as well as *N*D*k*-*m* symbols allow to make more precise identification of the coordination cores topologies. Hence, the *N*D*k*-*m* symbol for *e* is 2,3M6-1, while for *g* is 2,3,4M6-1.

The last member of the second group, the MST *j* $\{M_6(\mu\text{-}X)_6(\mu_3\text{-}X)_4\}$ is observed in three crystal structures of molybdenum S/Se/Cl-bridged compounds and can be viewed as combination of two trinuclear fragments bonded by four bridging atoms forming a close-packed hexanuclear core.

Notably, in all described MSTs, except MST *g*, the trimetallic $M_3(\mu\text{-}X)_2(\mu_3\text{-}X)$ fragments within the whole hexanuclear core are parts of incomplete cube-like $M_3(\mu\text{-}X)_3(\mu_3\text{-}X)$ moieties formed either by bridging atoms directly coordinated to $M_3(\mu\text{-}X)_2(\mu_3\text{-}X)$ fragments or bridges between them.

Table S3. Geometries of M_nX_m coordination cores, based on two $M_3(\mu\text{-}X)_2(\mu_3\text{-}X)$ fragments (shown as dark blue).

	MST	*N*D*k*-*m* symbol	Structure
e	$\{M_6(\mu\text{-}X)_7(\mu_3\text{-}X)_2\}$	2,3M6-1	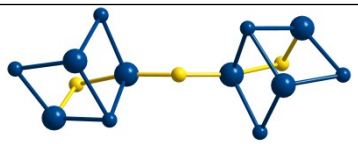
f	$\{M_6(\mu\text{-}X)_8(\mu_3\text{-}X)_2\}$	2,3M6-2	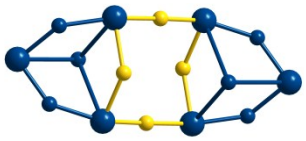
g	$\{M_6(\mu\text{-}X)_7(\mu_3\text{-}X)_2\}$	2,3,4M6-1	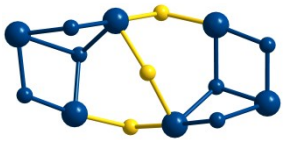
h	$\{M_6(\mu\text{-}X)_9(\mu_3\text{-}X)_2\}$	2,3M6-3	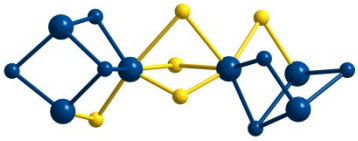
i	$\{M_6(\mu\text{-}X)_6(\mu_3\text{-}X)_2(\mu_4\text{-}X)\}$	2,4M6-1	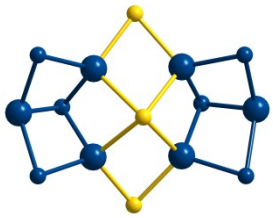

j	$\{M_6(\mu\text{-}X)_6(\mu_3\text{-}X)_4\}$	2,3,4M6-2	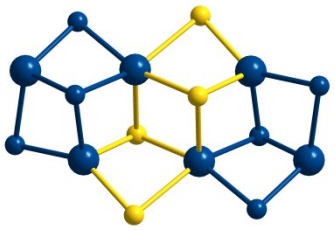

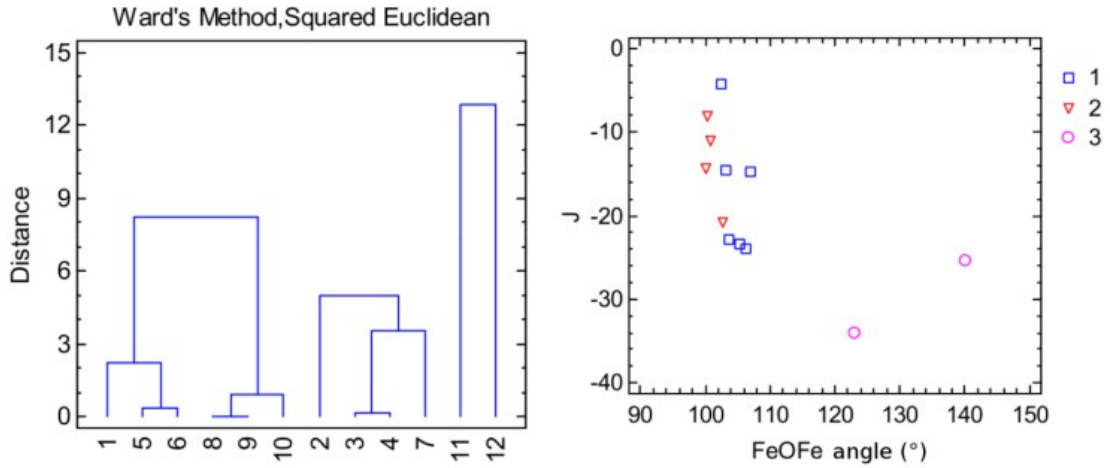

Figure S3. A dendogram of the Cluster Analysis (left) and the magnetostructural *J*-correlation (right) for hydroxido-bridged Fe(III) complexes. Numbers in the right corner are those of the respective clusters.

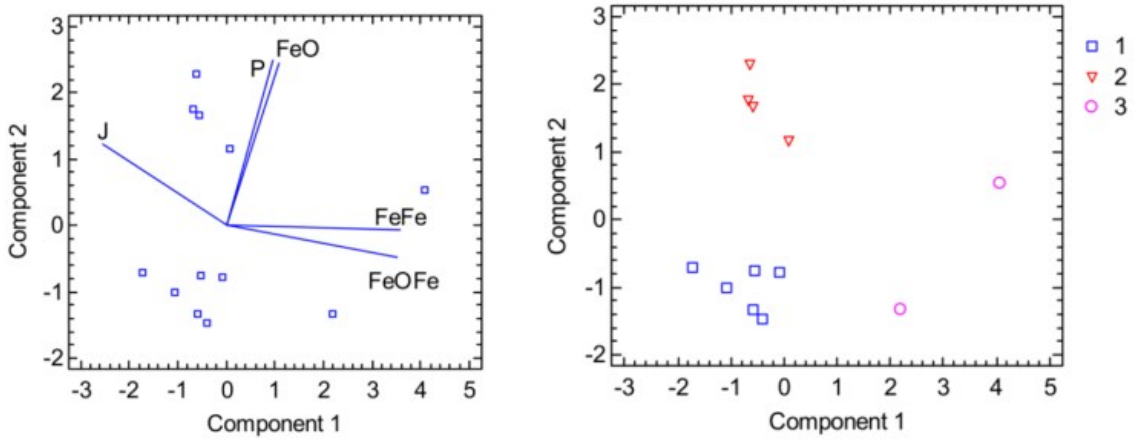

Figure S4. A biplot of the Principal Component Analysis for hydroxido-bridged Fe(III) complexes. Points are the objects (complexes) spanning the biplot. Numbers in the right corner are those of the respective clusters.

Correction of ^{18}O incorporation levels into tertiary cis- and trans-1,2-dimethylcyclohexanols in the experiment with $H_2{}^{18}O$

The mass-spectrometer PerkinElmer Clarus 600C (quadrupole mass analyser) was found to exhibit a non-linear decay of low-intensity mass-peaks, in some cases. For non-labeled *trans*- and *cis*-1,2-DMCH tertiary alcohols the 130/128 *m/z* ratio of 0.00568 can be predicted, from the natural abundance of $^{18}O/^{16}O$ isotopes. However, statistical data revealed considerable deviation of the 130/128 *m/z* ratio in the low intensity range (Figure S5). This statistics was accumulated from the data of different periods of time, calibrations, maintenance and does not seem to depend on these factors. The data were empirically fitted to the Hill equation

$$R = V\frac{{I_{130}}^n}{\left(k^n + {I_{130}}^n\right)}$$

where R is the observed 130/128 *m/z* ratio and I_{130} is the intensity of 130 *m/z* peak (these data correspond to species having natural ^{18}O abundance). The following coefficient values were found: $V = 0.3$, $k = 3 \times 10^{13}$, $n = 0.22$.

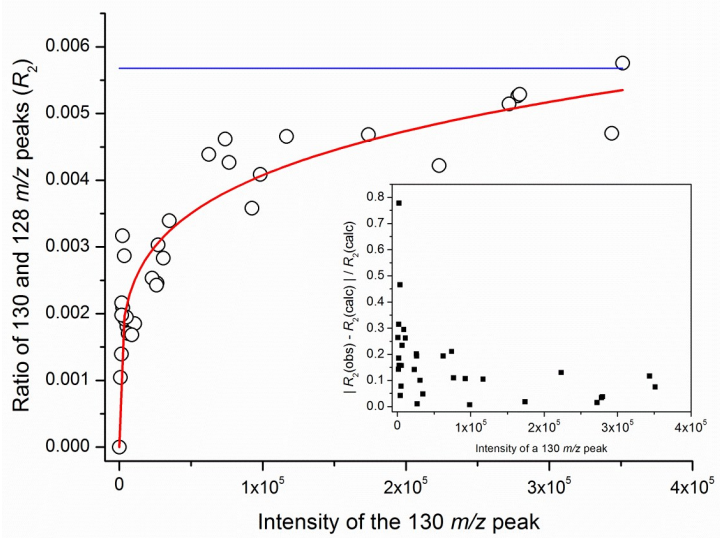

Figure S5. Dependence of 130/128 *m/z* intensities ratio on the 130 *m/z* peak intensity for non-labeled tertiary 1,2-DMCH alcohols. Theoretical 130/128 ratio is 0.00568 and is shown as a horizontal blue line. The inset shows the deviation of experimental data points from the empirical fit.

The final absolute intensities of 130 *m/z* peaks were estimated by applying the following correction:

$$I_{130Final} = I_{130}\frac{0.00568}{R} - I_{128}0.00568 = 0.00568\,V^{-1}(k^n\,{I_{130}}^{1-n} + I_{130}) - I_{128}0.00568$$

where I_{130} and I_{128} are experimentally observed absolute intensities of 130 and 128 *m/z* peaks, respectively. For the 130 *m/z* peaks having absolute intensity higher than 4.6×10^5 the 0.00568/R ratio was assumed to be equal to 1 (*i.e.* no correction is applied). The peaks of tertiary alcohols with intensity of 130 m/z peak lower than 2×10^4 were considered as not reliable due to very high scattering of experimental data in this region (Figure S5, inset). The intensities of 130 *m/z* peaks of *trans*-alcohols, obtained within the experiments with $H_2{}^{18}O$, fall completely into $0 - 2 \times 10^4$ region. Thus, the levels of ^{18}O in the *trans*-alcohol product and in the non-labeled compound are comparable and, therefore, cannot be reliably determined form the data collected. The initial data points for *cis*-alcohol (0 – 2 h reaction time) are also of low intensity (lower than 2×10^4), but since they fit well with the other data (Figure 10, inset) one may consider them as reliable.

Estimate of percentage of retention of stereoconfiguration (RC)

The RC value (in %) in oxidation of *cis*-substrate is typically estimated as

$$RC = \frac{(cis - trans)}{(cis + trans)} \times 100$$

where "*cis*" and "*trans*" are yields of tertiary *cis*- and *trans*-alcohols, respectively. RC of 100% corresponds to full retention of stereoconfiguration in the oxidation of *cis*-1,2-DMCH. However, a real substrate, *cis*-1,2-DMCH, always contains admixture of *trans*-1,2-DMCH, which should be taken into account when estimating RC. The commercial *cis*-1,2-DMCH contained 1.8% of *trans*-1,2-DMCH. Hence, the RC value (in %) can be calculated as

$$RC = \frac{(cis - trans + 0.018cis)}{(cis + trans - 0.018cis)} \times 100$$

Figures (plots, chromatograms and mass-spectra)

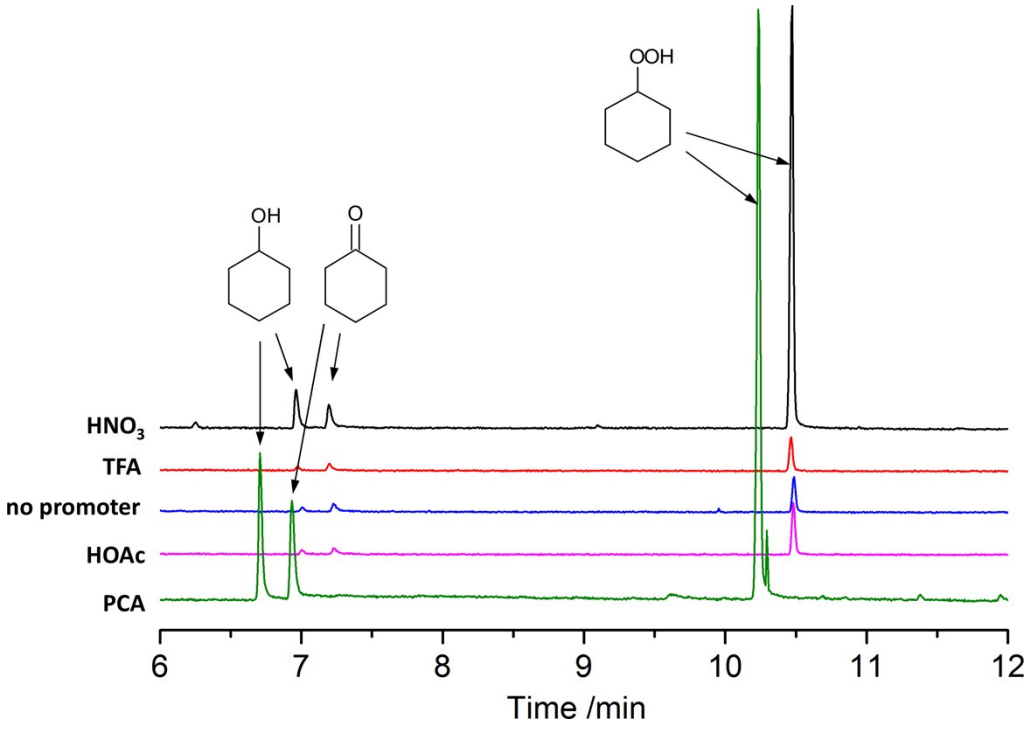

Figure S6. Fragments of the chromatograms of the reaction samples (from the cyclohexane oxidation in the presence of various promoters) taken at 120 min time and recorded before addition of PPh_3 (SGE BPX-5 column). GC analysis of the reaction sample with PCA promoter was performed under slightly different conditions, thus revealing different retention times.

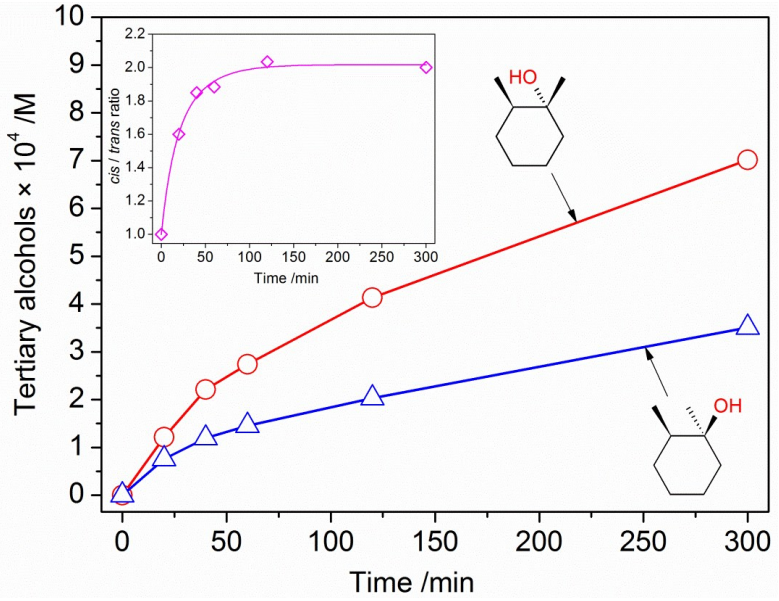

Figure S7. Accumulations of main products (tertiary *cis*- and *trans*-alcohols) in the course of *cis*-1,2-DMCH oxidation (0.1 M) with *m*-CPBA (0.027 M) catalysed by the complex **1** (4.1×10^{-4} M) in the presence of HNO_3 (5.5×10^{-3} M) in acetonitrile at 50 °C. Insets show the dependences of *cis*/*trans* ratios (ratios of tertiary *cis*- and *trans*-alcohols) with the time.

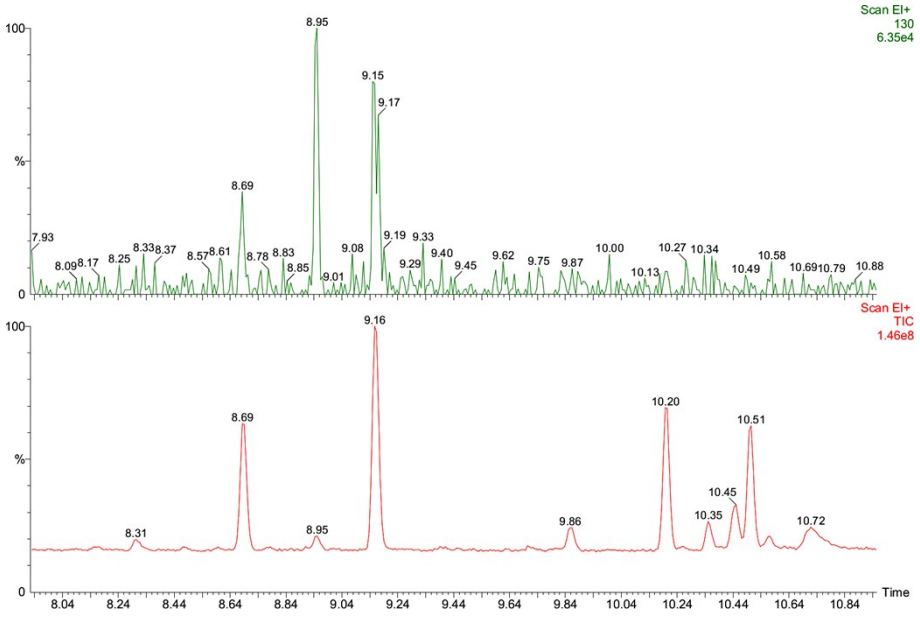

Figure S8. Fragment of the chromatogram (top: 130 *m/z* signal; bottom: summary signal), showing the reaction products in the course of *cis*-1,2-DMCH oxidation with *m*-CPBA, in the presence of HNO_3 and $H_2{}^{18}O$, catalysed by the complex **1** (recorded at 6 h time after addition of PPh_3; SGE BPX-5 column). Assignments of the known peaks (mins): 8.69 and 9.16, tertiary *trans*- and *cis*-alcohols; 8.95, 2-octanone; 10.20, 2,3-dimethylcyclohexanone; 10.35, 2,3-dimethylcyclohexanol; 10.45, 3,4-dimethylcyclohexanol; 10.51, 3,4-dimethylcyclohexanone.

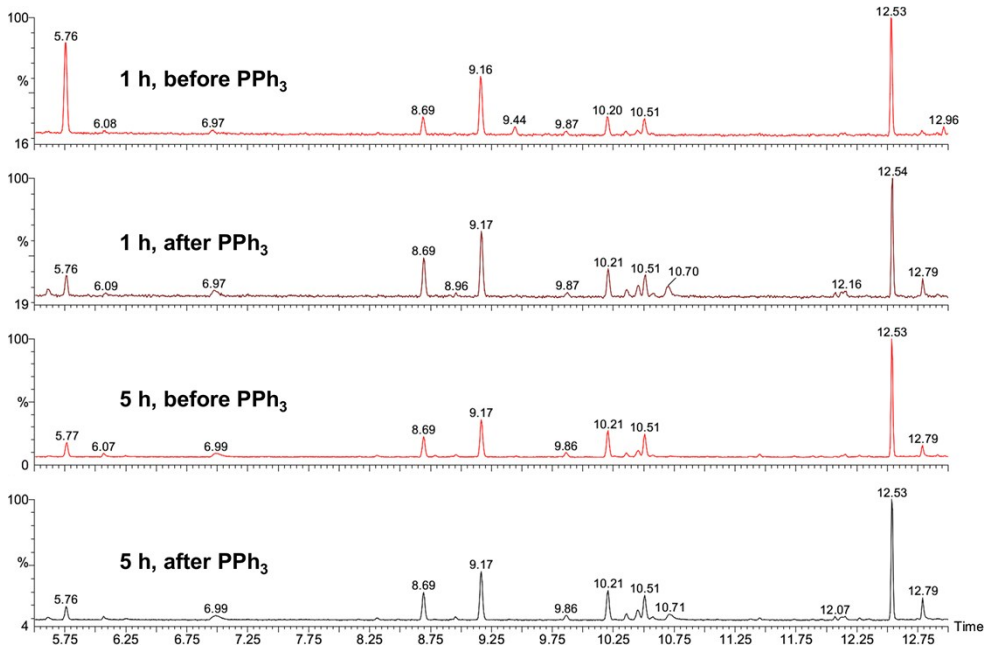

Figure S9. Fragments of the chromatograms, showing the reaction products in the course of *cis*-1,2-DMCH oxidation with *m*-CPBA, in the presence of HNO_3 and $H_2{}^{18}O$, catalysed by the complex **1** (chromatograms recorded before and after addition of PPh_3; SGE BPX-5 column). Assignments of the peaks in the range 8–11 mins are as those on Figures S8 and S10. Assignments of the other peaks (mins): 5.76, chlorobenzene; 12.53, 2,7-octanedione.

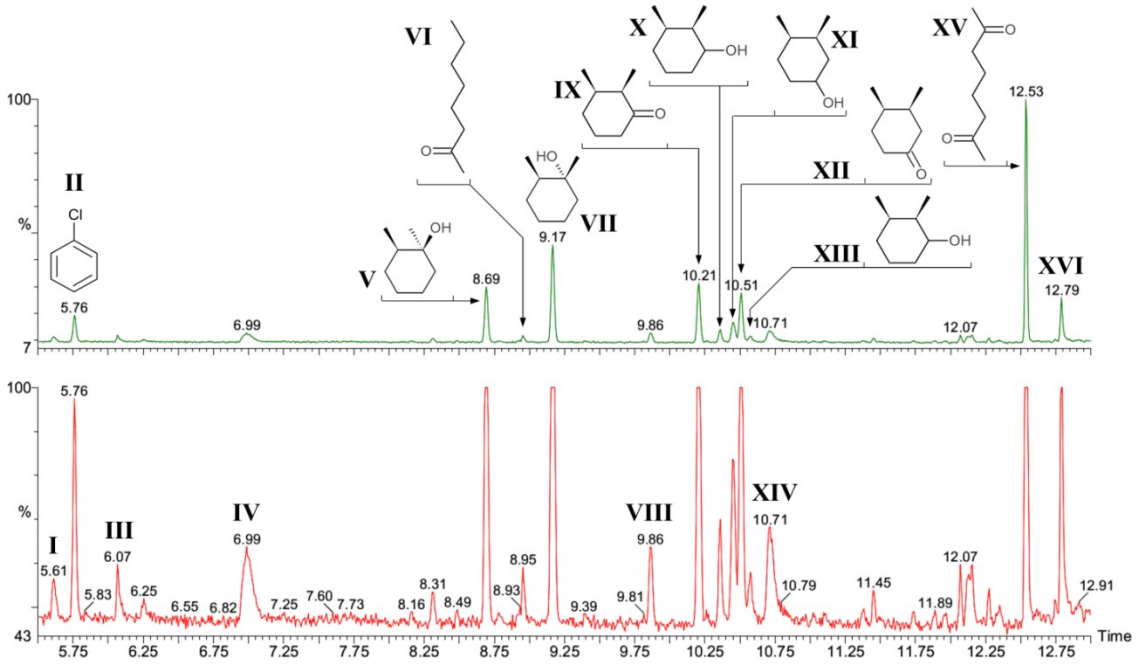

Figure S10. Fragment of the chromatogram (top and bottom show different intensity scales) of the reaction (by-)products in the oxidation of *cis*-1,2-dimethylcyclohexane with *m*-CPBA catalyzed by complex **1** in the presence of HNO_3 in acetonitrile at room temperature and 24 h reaction time.

Figures S11: The following figures represent EI mass-spectra of the peaks **I–XVI** (Figure S10), measured in the catalytic tests performed in the absence (top, green) and presence (bottom, red) of $H_2{}^{18}O$.

Peak **I**:

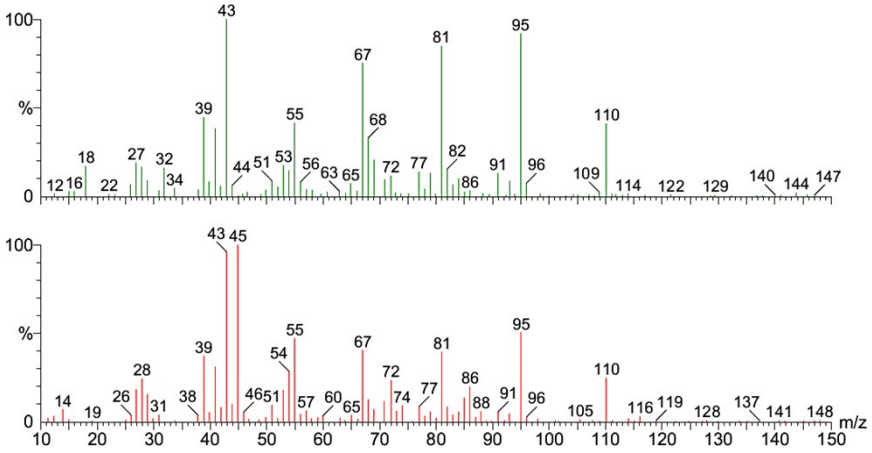

Peak **III**:

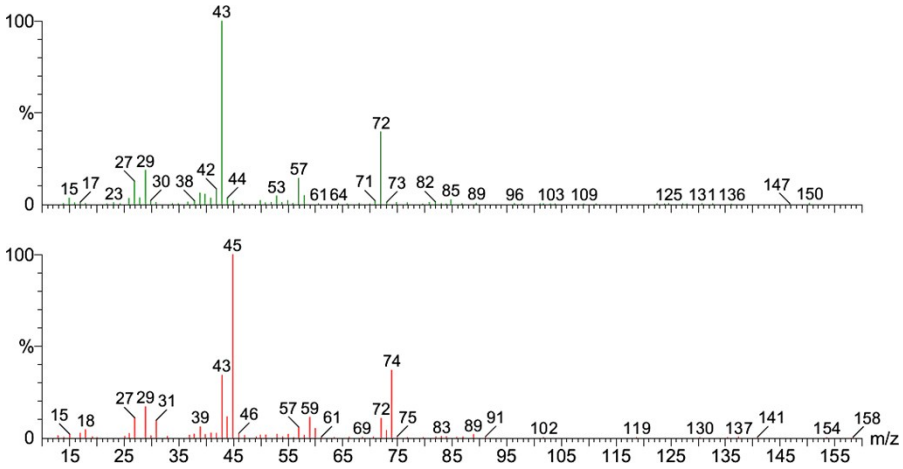

Peak **IV**:

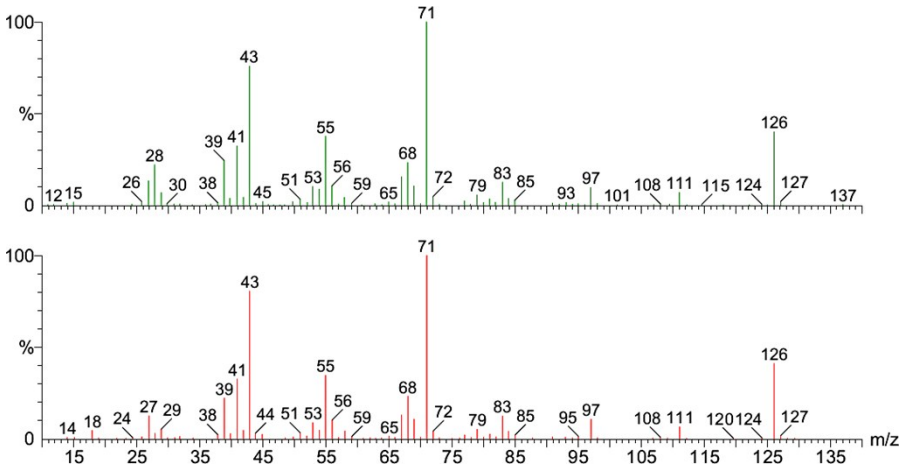

Peak **V**:

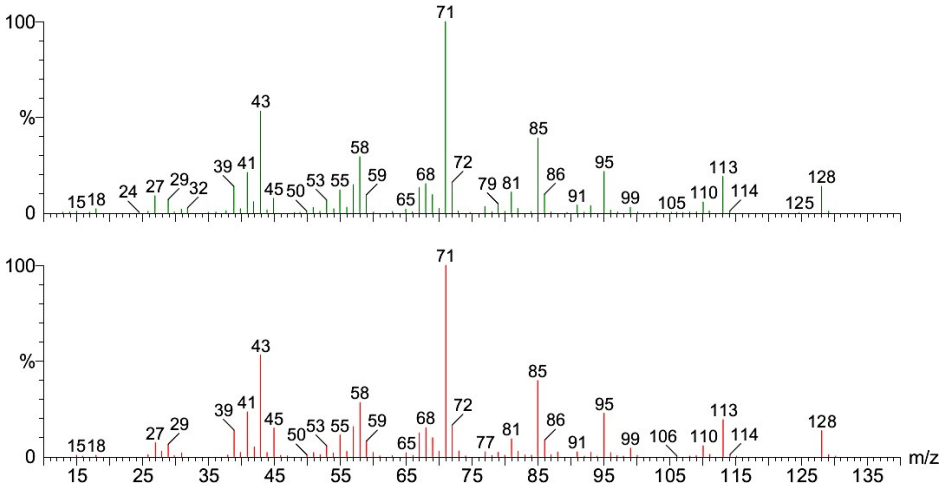

Peak **VI**:

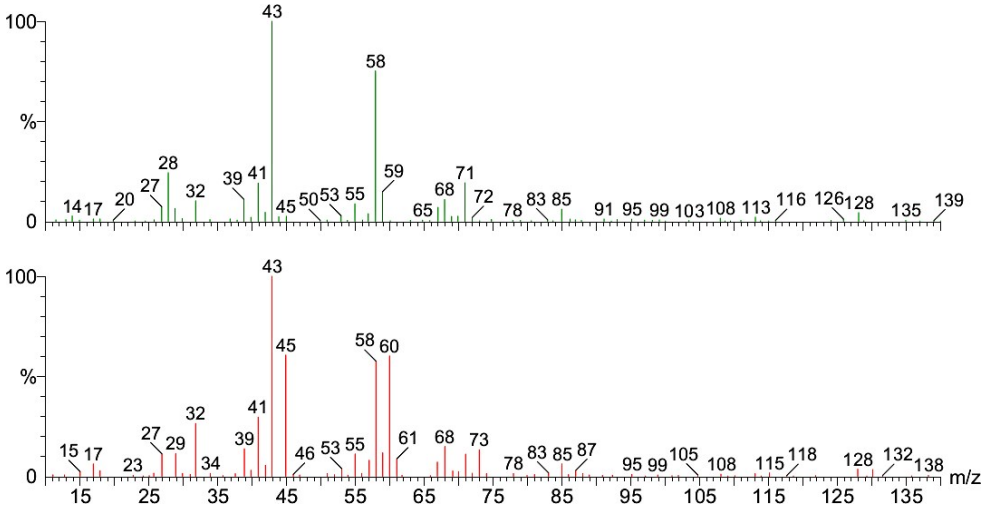

Peak **VII**:

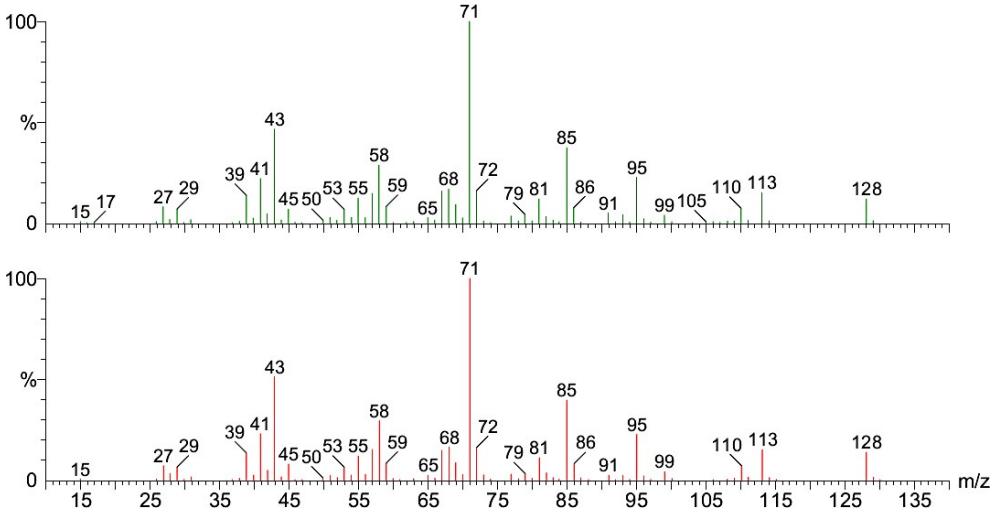

Peak **VIII**:

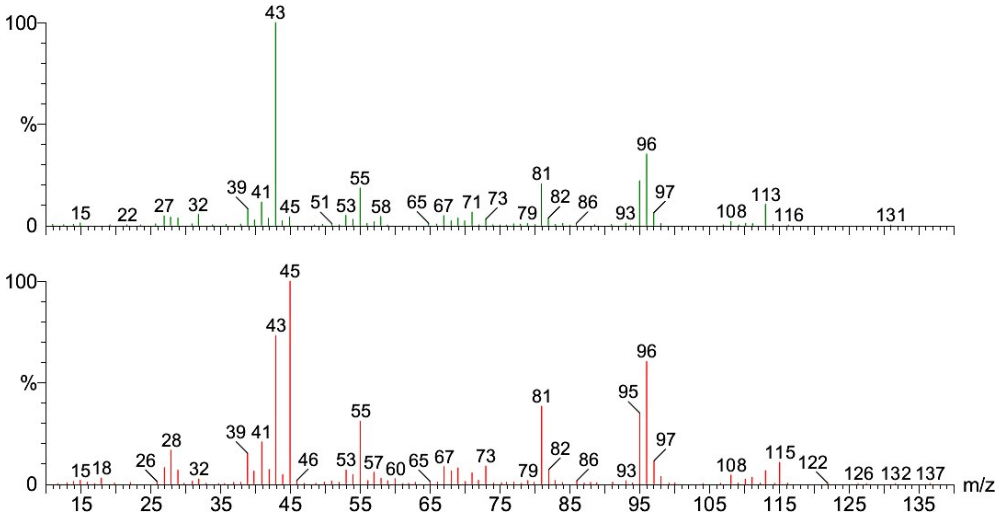

Peak **IX**:

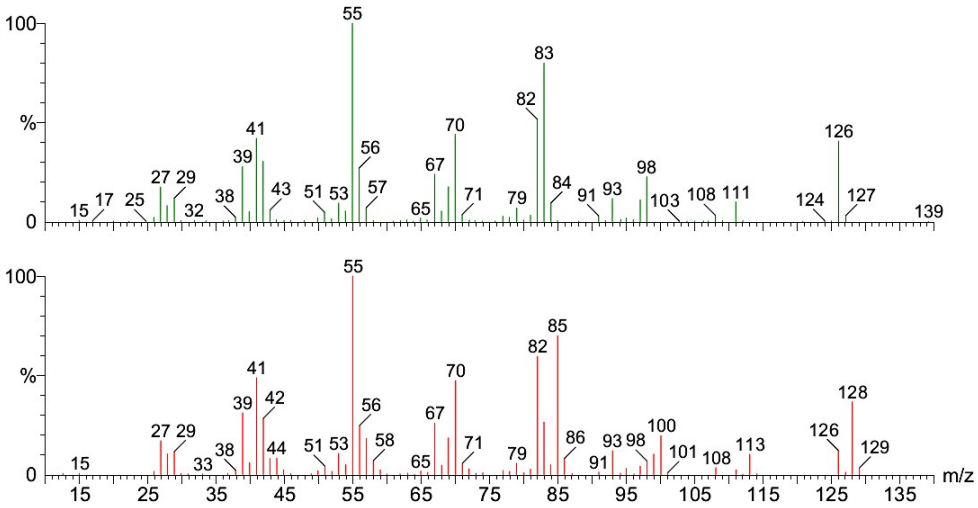

Peak **X**:

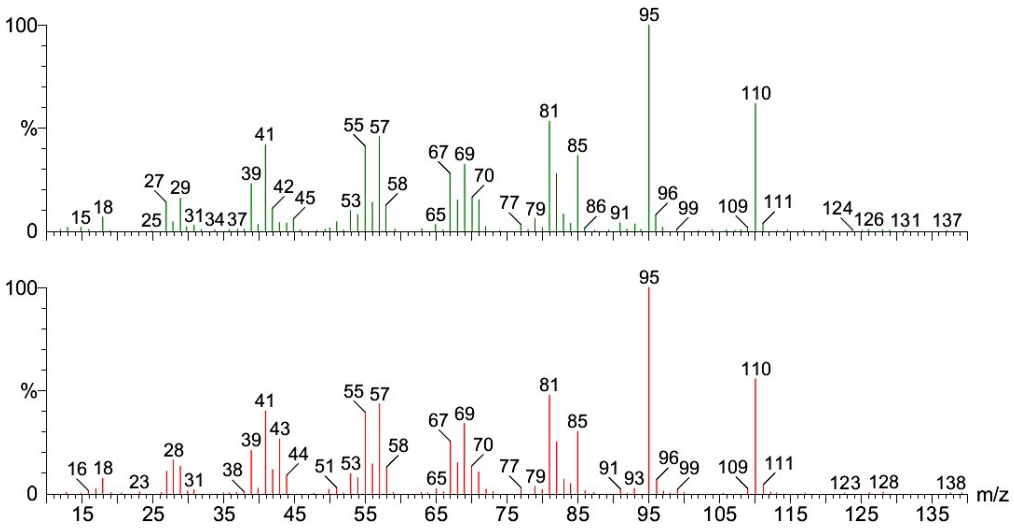

Peak **XI**:

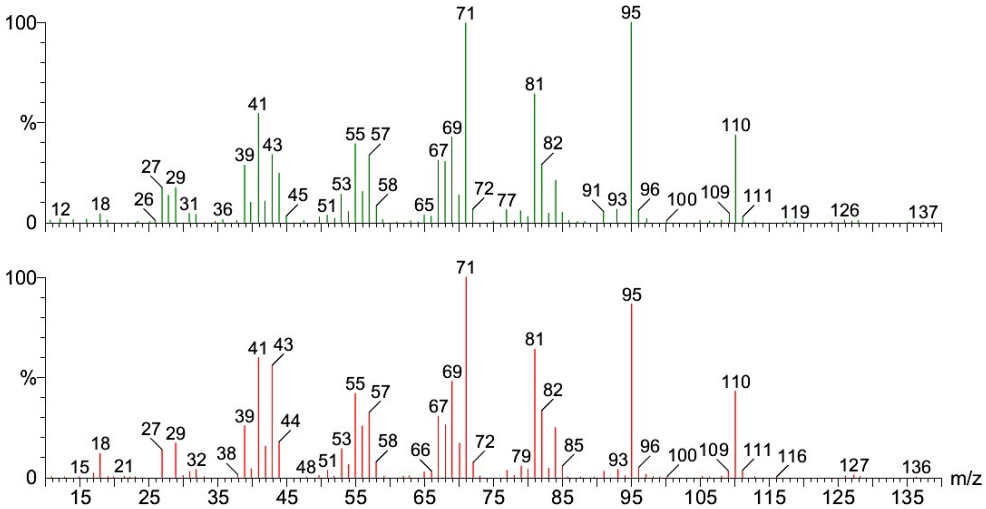

Peak **XII**:

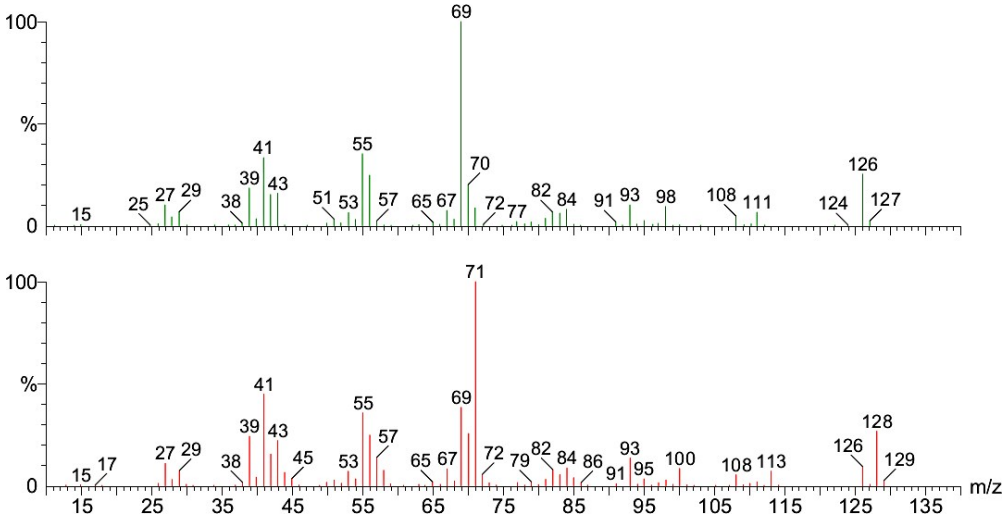

Peak **XIII**:

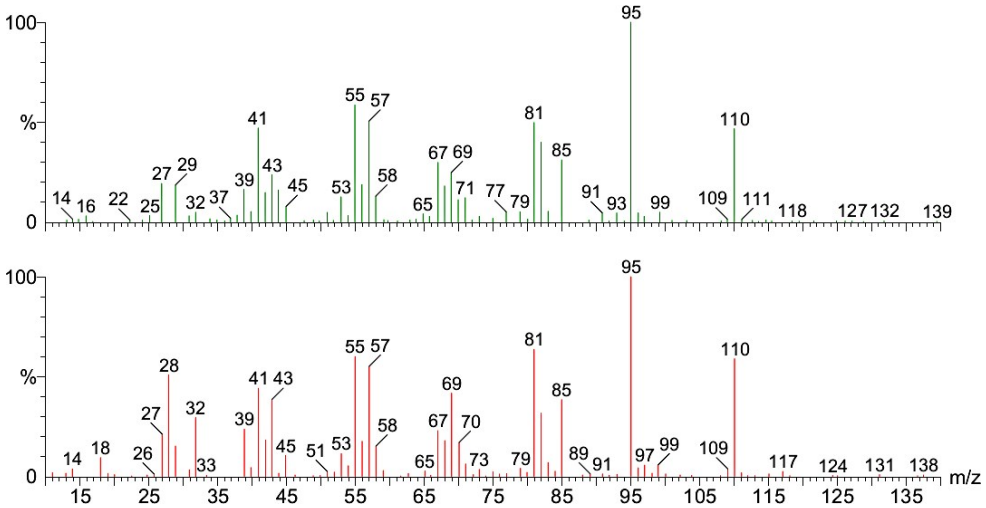

Peak **XIV**:

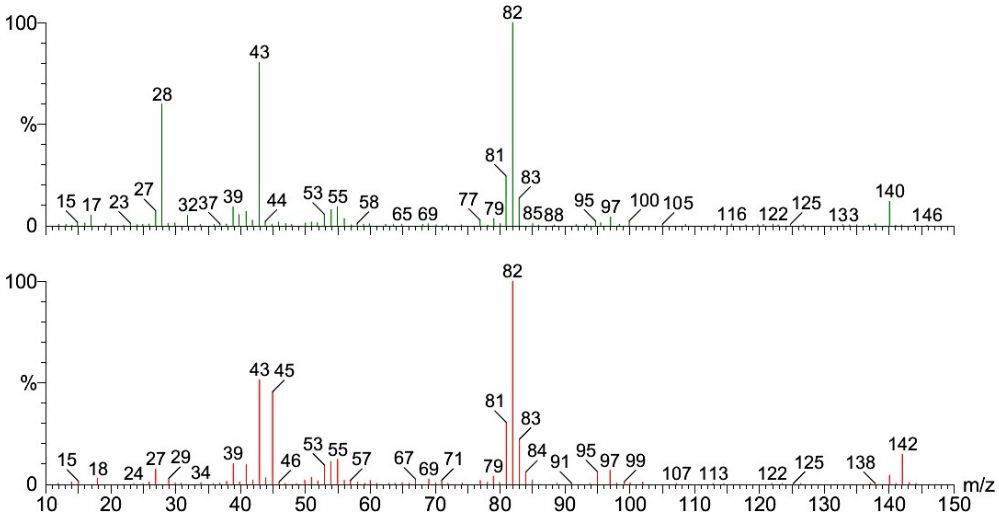

Peak **XV**:

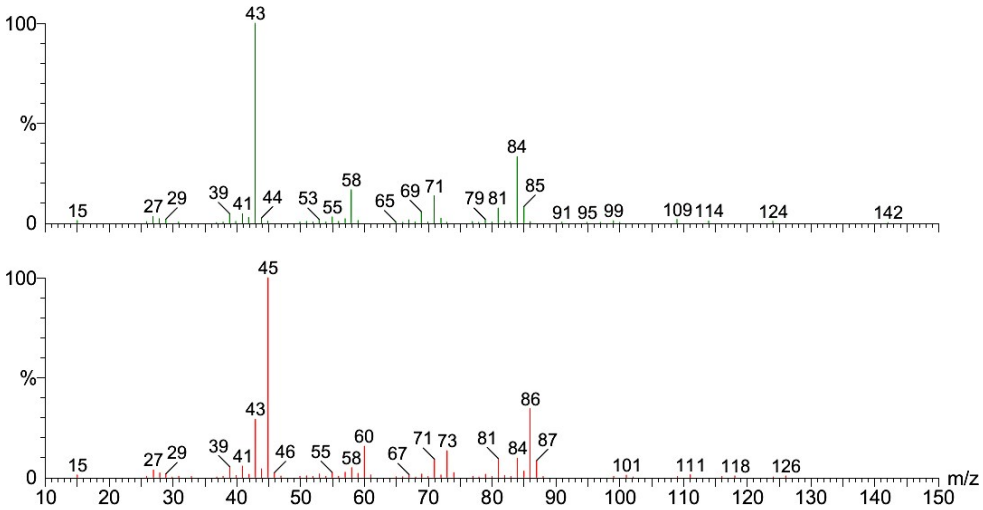

Peak **XVI**:

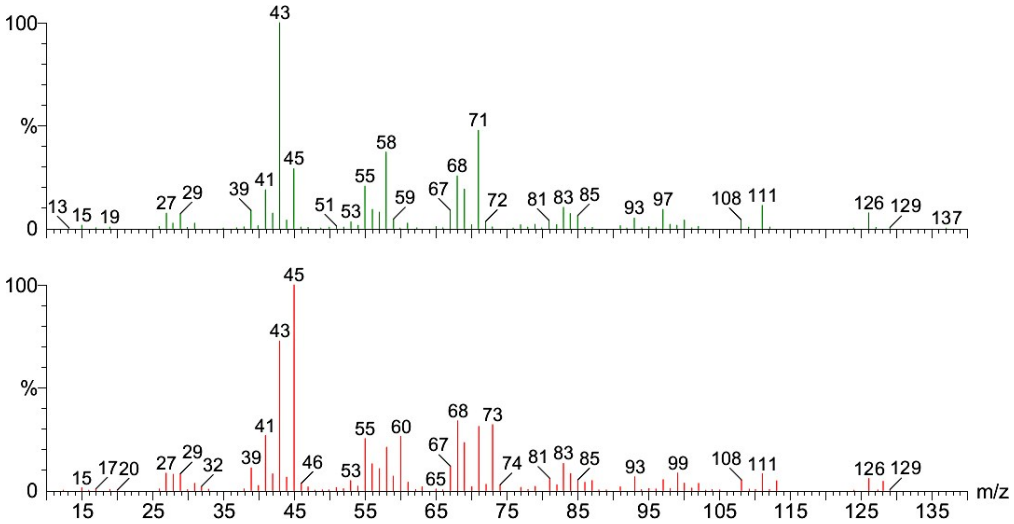

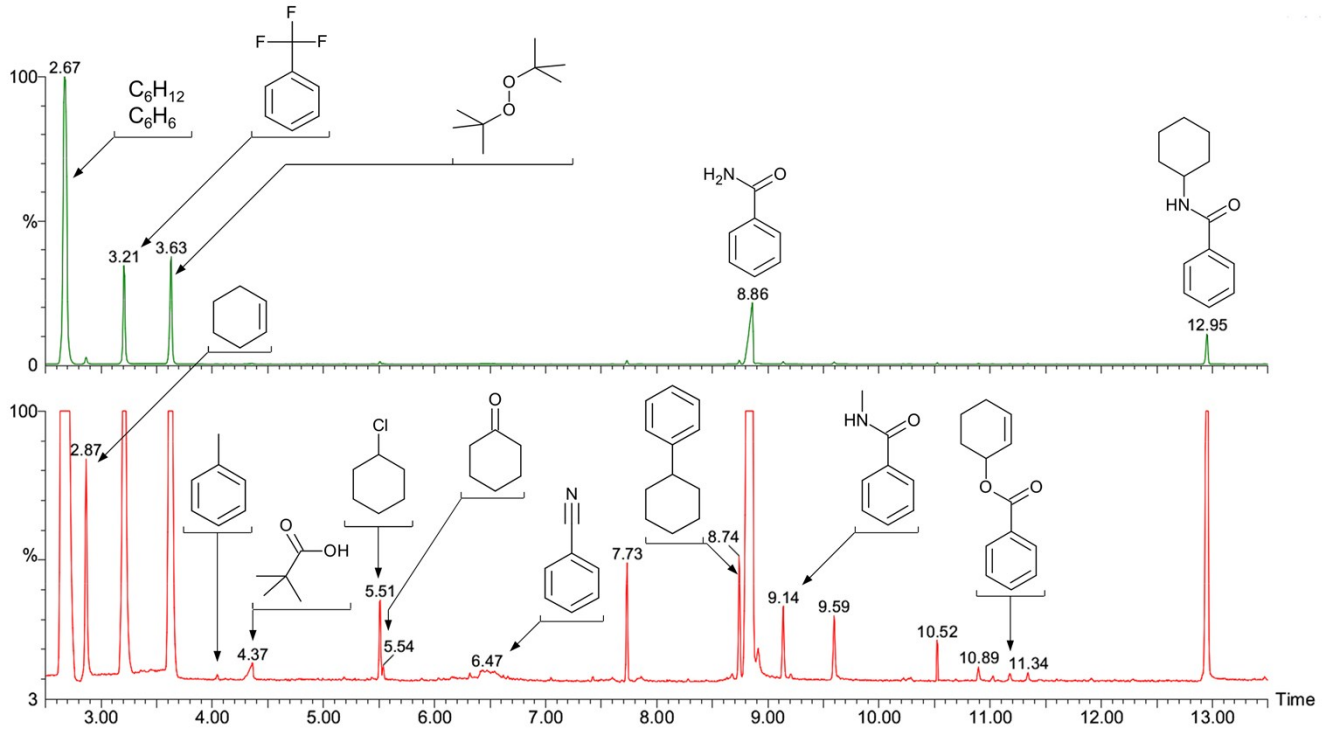

Figure S12. Fragment of the chromatogram (top and bottom show different intensity scales) of the reaction (by-)products in the oxidative amidation of cyclohexane with benzamide, in the presence of ^{t}BuOO^{t}Bu, catalyzed by complex **1** in benzene at room temperature and 24 h reaction time. The mass-spectrum of the peak at 7.73 min (Fig. S13) was not identified, while that of the peak at 9.59 min suggests (Fig. S14) its correspondence to a derivative of benzamide with molecular weight of 149 g mol^{-1} (according to the highest *m/z* peak in the mass-spectrum).

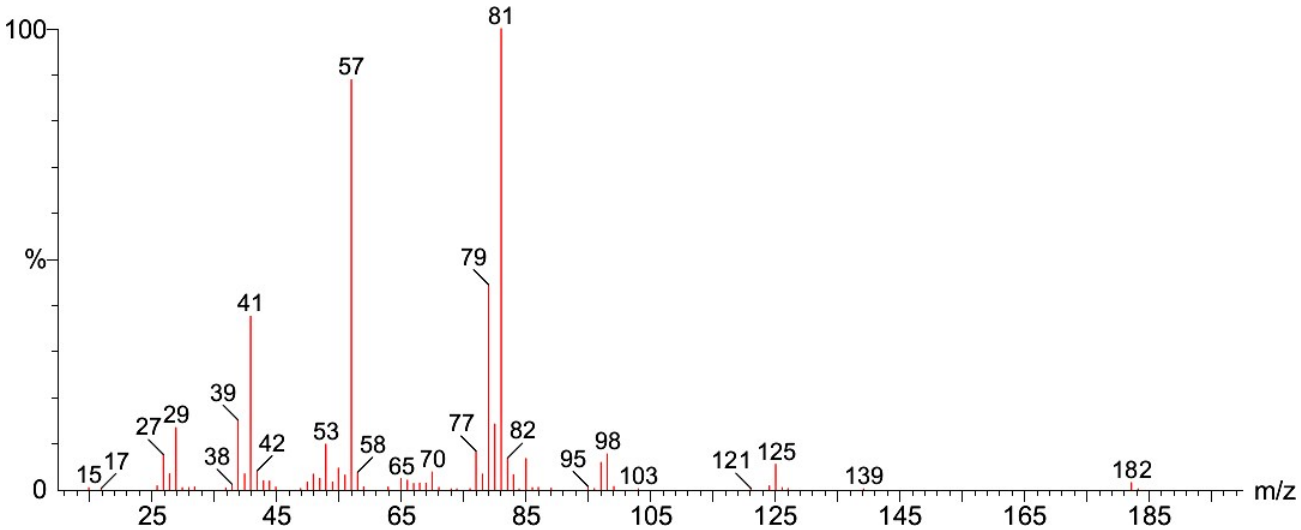

Figure S13: EI mass-spectrum of the peaks at 7.73 min from the chromatogram depicted at Figure S12.

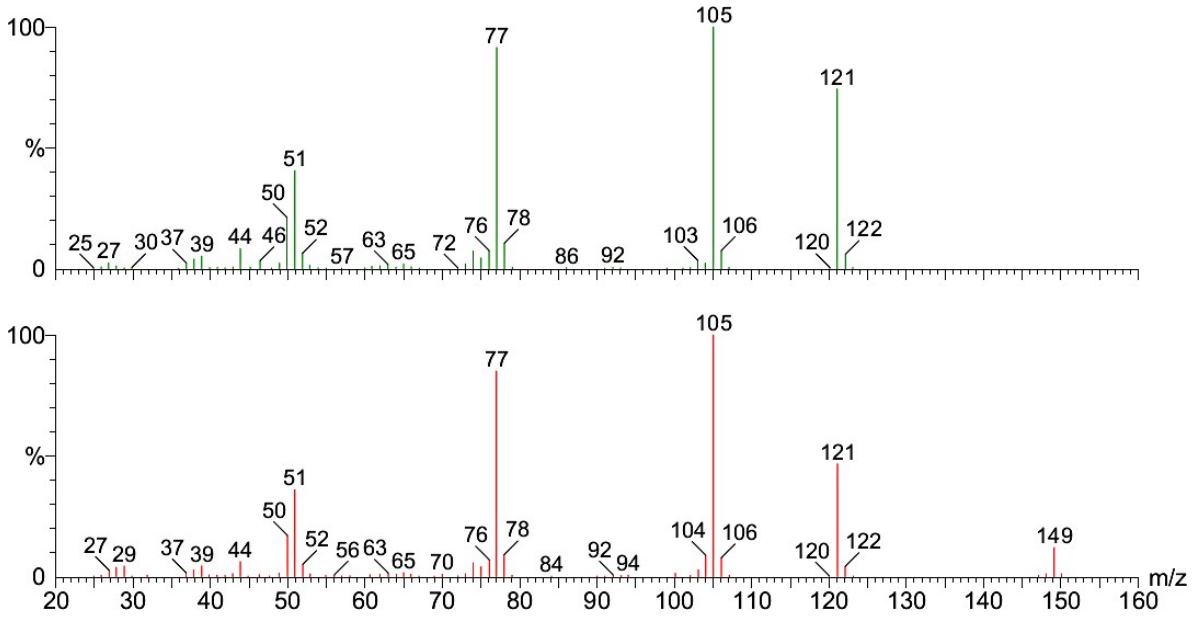

Figure S14: Bottom: EI mass-spectrum of the peaks at 9.59 min from the chromatogram depicted at Figure S12. Top: EI mass-spectrum of benzamide.

References

1. (a) D. S. Nesterov, O. V. Nesterova, V. N. Kokozay and A. J. L. Pombeiro, *Eur. J. Inorg. Chem.*, 2014, 4496-4517; (b) V. G. Kessler, *Chem. Commun.*, 2003, 1213-1222.
2. C. R. Groom and F. H. Allen, *Angew. Chem. Int. Ed.*, 2014, **53**, 662-671.
3. (a) Z. H. Li, P. Lin and S. W. Du, *J. Mol. Struct.*, 2008, **892**, 182-187; (b) R. Wang, L. L. Song, K. Y. Hu, Q. H. Jin and C. L. Zhang, *Acta Crystallogr. E*, 2010, **66**, M1185-U1187.
4. J. Y. Niu, X. Q. Zhang, D. H. Yang, J. W. Zhao, P. T. Ma, U. Kortz and J. P. Wang, *Chem. Eur. J.*, 2012, **18**, 6759-6762.
5. F. A. Cotton, R. Llusar and W. Schwotzer, *Inorg. Chim. Acta*, 1989, **155**, 231-236.
6. (a) W. Clegg, R. J. Errington, D. C. R. Hockless and C. Redshaw, *Polyhedron*, 1989, **8**, 1788-1789; (b) J. Zhao and L. Xu, *Eur. J. Inorg. Chem.*, 2011, 4096-4102.
7. M. Hashimoto, T. Iwamoto, H. Ichida and Y. Sasaki, *Polyhedron*, 1991, **10**, 649-651.
8. K. Moriwaki, R. Yoshida and H. Akashi, X-ray Structure Analysis Online, 2014, 30, 11-12.
9. (a) G. E. Kostakis, V. A. Blatov and D. M. Proserpio, *Dalton Trans.*, 2012, **41**, 4634-4640; (b) G. E. Kostakis and A. K. Powell, *Coord. Chem. Rev.*, 2009, **253**, 2686-2697; (c) E. A. Buvaylo, O. V. Nesterova, V. N. Kokozay, O. Y. Vassilyeva, B. W. Skelton, R. Boca and D. S. Nesterov, *Cryst. Grow. Des.*, 2012, **12**, 3200-3208.